Available online at www.sciencedirect.com
SCIENCE DIRECT®
Journal of Solid State Chemistry 170 (2003) 9–23
JOURNAL OF SOLID STATE CHEMISTRY
http://elsevier.com/locate/jssc

Effects of oxygen nonstoichiometry and of its distribution on Verwey-type transitions and structure of $GdBaFe_2O_{5+\bar{w}}$

P. Karen

Department of Chemistry, University of Oslo, P.O. Box 1033 Blindern, N-0315 Oslo, Norway

Received 20 February 2002; received in revised form 4 June 2002; accepted 15 July 2002

Abstract

Evolutions of the mixed-valence (MV) and charge-ordered (CO) phases of $GdBaFe_2O_{5+\bar{w}}$ are investigated as a function of $\bar{w}(-0.02<\bar{w}<0.40)$ by differential scanning calorimetry (DSC) and synchrotron X-ray powder diffraction. Whereas the oxygen nonstoichiometry level $\bar{w}$ follows from cerimetric titrations, the oxygen content distribution $X(w)$ is evaluated from deconvolutions of Bragg-peak broadenings. The somewhat tailed $X(w)$ does not change between the CO and MV phases, but increases as a function of the $\bar{w}$ level. This suggests synthesis as its main origin. Below $\bar{w}=0.23$, the discontinuous CO/MV Verwey transition appears, showing a hysteresis as well as a temperature range where the CO and MV phases coexist, differing in the degree of orthorhombic distortion and molar volume. Convolutions with the $\bar{w}$ dependence of the transition temperature T_V indicate that the coexistence is largely owing to $X(w)$, resulting in different parts of the sample having slightly different T_V. Below $\bar{w}=0.04$, a premonitory charge-ordering transition is registered by DSC, having no detectable structural effect. Below $\bar{w}\approx 0.02$, a 3D long-range order of charges of the $TbBaFe_2O_5$-type appears. For a $\bar{w}=-0.001$ composition, 21 weak superstructure Bragg reflections is visually identified. Intensity resolution for several of them depends heavily on fine modeling of the main-peak footings affected by two types of oxygen disorder: $X(w)$ and a residual tetragonal disorder. Both are successfully simulated by a multiple-phase Rietveld refinement. Thermodynamic parameters of the two transitions at the ideal composition with $\bar{w}=0$ are evaluated from composition dependences.

Keywords: Mixed valence; Charge ordering; First-order transition; Nonstoichiometry distribution; Transition thermodynamics; Rare-earth barium iron oxides

1. Introduction

Iron is the only transition element for which both double- and triple-cell perovskite of the same constituent elements have been obtained. This coincidence provides interesting comparisons. In the triple-cell perovskite $YBa_2Fe_3O_8$, one single valence state of iron is maintained despite presence of two types of iron coordination polyhedra [1]. The double-cell perovskite $YBaFe_2O_5$ experiences a converse task: two integer valences are to be accommodated in just one type of coordination polyhedron [2]. As it turns out, the solution to the latter parsimony problem is temperature dependent. Whereas at low temperatures *integer* valences are preferred and a structural ordering into two deformed Fe^{2+} and Fe^{3+} square pyramidal coordinations appears, at high temperatures, the *integer* structure prevails, having just one single type of the coordination square-pyramid owing to the valence mixing into the $Fe^{2.5+}$ state [3,4]. The freezing of the mixed-valence (MV) electrons into the localized, charge-ordered (CO) state appears as a diffusionless, first-order transition and is preceded by a weak premonitory effect. The latter utilizes the existing structural distortion associated with the antiferromagnetic (AFM) order to partially split the single MV state [4]. When the final ordering is made possible by a further decrease in temperature, it happens so under all symptoms of the classical Verwey transition [5]: electrical conductivity increase, exothermic thermal effect, volume increase and a profound structural deformation that all accompany the electron localization and ordering [4,6]. Within the overall AFM order, the classical double-exchange mechanism appears to play the same role as in magnetite, since a ferromagnetic coupling appears in the MV phase between pairs of iron atoms across the Y layer [4]. In the CO phase, also this

E-mail address: pavel.karen@kjemi.uio.no (P. Karen).

0022-4596/03/$ - see front matter © 2002 Elsevier Science (USA). All rights reserved.
PII: S0022-4596(02)00008-7

coupling becomes AFM. This interaction helps to explain changes in the transition temperature and caloric effects observed when Y is exchanged for another rare-earth (R) atom [4,6].

In general, decreasing size of R undermines the ability to accommodate the added oxygen $\bar{w}$ [2,4], and the $R = \mathrm{Gd}$ variant is the last one having a wide non-stoichiometry range. Verwey transition parameters of $GdBaFe_2O_{5+\bar{w}}$ are investigated in this study by means of synchrotron X-ray powder diffraction and calorimetric measurements. Since the Verwey-type charge ordering is sensitive to slightest departures from ideal stoichiometry [7], a special attention is paid here to the control and characterization of the oxygen nonstoichiometry, including distribution of the oxygen content across the bulk. The latter is often being neglected when we treat nonstoichiometric samples as being sharp compositions.

2. Experimental

2.1. Synthesis

The master sample was synthesized from a nanoprecursor obtained by liquid mixing in a citrate melt. Annealed Gd_2O_3 (99.99%, Stanford Materials, ~ 15 g) was dry-mixed with 300 g of high-purity citric acid monohydrate (Fluka, $<0.02\%$ sulfate ash) and dissolved upon melting assisted by some 10 mL of water added at the bottom of the beaker. Iron (lumps, 99.95%, Koch-Light) was dissolved in dilute HNO_3 and added into the melt still containing enough water to prevent an immediate rapid development of nitrous gases. Upon continued warm-up and stirring, most of nitrate ions were removed in this manner. After cooling below 100°C, some 100 mL of distilled water was added, and barium carbonate (Fluka, $<0.2\%$ Sr) was dissolved. A clear viscous melt was obtained under evaporation of excess water and subsequently decomposed into a porous organic-based solid at 180°C. The solid was pulverized and incinerated for 5 days in a covered porcelain crucible at 400°C into an extremely fine, X-ray amorphous powder. After calcination and homogenization in a vibration mill, the cold-pressed powder (150 kg/cm^2) was sintered under conditions listed in Table 1 into silvery black cylinders (~ 6 mm in diameter) of practically full density thanks to the nanoprecursor. The product was single phase according to synchrotron powder X-ray diffraction.

Table 1
Synthesis conditions of the $GdBaFe_2O_{5+\bar{w}}$ master sample

	t (°C)	Ar/H_2	$\log(pH_2O/\mathrm{bar})$	$\log(p_{O_2}/\mathrm{bar})$
Calcination	900	156	−1.67	−15.09(9)
Sintering	1000	16.5	−1.60	−15.14(2)

2.2. Oxygen content control, analysis and characterization

The oxygen nonstoichiometry was controlled by high-temperature equilibration and quenching in atmospheres of hydrogen, water and argon. Mixtures of 10% H_2 in Ar (5 N, with analysis certificate) and Ar (4 N) were used as flowing reaction atmospheres either directly or after wetting in a saturated solution of KBr of known temperature. Partial pressures of the components were calculated from thermodynamic data, except for H_2O contents in the range of ppm, when an Endress–Hauser MMY150 hygrometer was used. After 5–7 days of equilibration, samples were quenched into a bulk metal container inside the synthesis line, filled with high-purity Ar (<2 ppm O_2) dried over a P_2O_5 desiccant. Samples were stored under argon, and a thin surface layer was removed before further characterizations. Oxygen contents were determined by cerimetric titrations in duplicate or triplicate [8], and are listed in Table 2 together with details on quenching conditions and unit-cell parameters obtained by conventional powder X-ray diffraction (Guinier–Hägg camera, Cu$K\alpha_1$, Si internal standard). The sample with $\bar{w} = 0.013$ was synthesized in bulk, crushed and separated into a series of fractions with particle sizes between $22, 36, 45, 100$ and 200 μm in an Ar-filled vibration-sieve column.

2.3. Differential scanning calorimetry (DSC)

A liquid-nitrogen operated Perkin–Elmer Pyris 1 instrument was used to register thermal flux curves upon heating (10 K/min) between 170 and 340 K. Aluminum pans (50 μL, 50 mg) were used to seal the powdered samples of typically 70–90 mg weight. Peak temperatures were corrected to the zero sample-weight based on a separate calibration series (20–140 mg). Also the effect of the particle size was tested and found insignificant. The temperature scale was calibrated on cyclopentane, cyclohexane, *n*-octane, *n*-decane, *n*-dodecane, *m*-nitrotoluene and *p*-nitrotoluene standards of $>99.7\%$ purity and found completely linear. Enthalpy was standardized on melting of (the Perkin–Elmer) indium, and the calibration was verified through an agreement with low-temperature phase transitions of cyclohexane. The background was reconstructed from peak-free regions by fitting with a polynomial curve of suitably high order.

2.4. Synchrotron X-ray powder diffraction (SXPD)

Data were collected at a two-circle powder diffractometer equipped with helium-operated cryostat, as

Table 2
Nonstoichiometry control and characterizations of used $GdBaFe_2O_{5+\bar{w}}$ samples

$5+\bar{w}$	a (Å)	b (Å)	c (Å)	Ar/H_2	$\log(p_{H_2O}/bar)$	$\log(p_{O_2}/bar)$	t (°C)
4.980(2)	3.9543(5)	3.9348(5)	7.5914(15)	8.65(0)	−4.3	−29.36(1)	620
4.985(1)	3.9534(8)	3.9346(8)	7.5901(15)	8.65(0)	−4.4	−29.28(1)	630
4.996(1)	3.9550(4)	3.9344(4)	7.5912(11)	8.65(0)	−4.4	−30.15(1)	610
4.999(3)	3.9551(5)	3.9340(4)	7.5919(10)	8.65(0)	−4.4	−30.08(1)	605
5.004(2)	3.9524(7)	3.9350(7)	7.5904(12)	8.78(0)	−4.1	−28.86(1)	630
5.010(3)	3.9550(9)	3.9337(10)	7.5922(15)	9.19(0)	−4.0	−29.36(1)	610
5.013(2)	3.9545(5)	3.9354(6)	7.5922(13)	8.52(0)	−1.74	−15.95(2)	1000
5.014(5)	3.9550(5)	3.9334(5)	7.5898(12)	8.78(0)	−4.1	−29.18(1)	620
5.017(2)	3.9548(6)	3.9342(6)	7.5917(14)	22.2(5)	−4.0	−28.91(1)	600
5.028(2)	3.9540(7)	3.9339(5)	7.5920(9)	33.3(5)	−1.78	−14.92(3)	1000
5.041(1)	3.9534(5)	3.9347(5)	7.5988(12)	64(1)	−1.79	−14.39(1)	1000
5.061(1)	3.9486(8)	3.9370(7)	7.6057(15)	82(2)	−1.76	−14.11(1)	1000
5.096(4)	3.9410(4)		7.6157(10)	123(3)	−1.70	−13.63(1)	1000
5.113(1)	3.9407(2)		7.6214(6)	198(6)	−1.74	−13.28(4)	1000
5.181(1)	3.9385(2)		7.6452(5)	333(18)	−1.70	−12.75(6)	1000
5.300(1)	3.9354(4)		7.6834(10)	880(137)	−1.70	−11.87(14)	1000
5.392(2)	3.9322(3)		7.7114(9)	1788(42)	−1.65	−11.05(3)	1000

Note. Ratio Ar/H_2 is by volume and standard error of mixing refers to variations over time.

installed on the BM1B beamline at the ESRF Grenoble. Temperature readings were self-consistent: calibrated at the inflection points of the transition curves of the measured samples, the peak transition temperatures being known from DSC. Samples sealed under argon in glass capillaries (0.25 mm diameter) were rotated in the monochromatic X-ray beam with a cross-section $1 \times 5\ mm^2$ and $\lambda \approx 0.5$ or ≈ 0.6 Å. A NIST standard silicon was used to determine the wavelength λ and the zero-point correction. High-intensity data for structure refinements of the CO crystal structure of $GdBaFe_2O_{4.999}$ were collected at 100 K (a nominal temperature) with detector setup having six Si(1 1 1) analyzer crystals and NaI scintillation counters (separated by $\sim 1.1^\circ$ 2θ). A step of 0.002° 2θ and a counting time of 4–5 s were used for the scans over the angular range of $4^\circ < 2\theta < 40^\circ$. Data for structure refinements of the low-temperature samples with varied oxygen nonstoichiometry were recorded at 182 K over a shorter angular range with a quadruplet of Si(1 1 1) analyzers. Short isothermal scans were then performed on the same samples between the calibrated temperatures of 182 and 302 K over the narrow angular range of the 1 0 0, 0 1 0, 0 0 2 or 2 0 0, 0 2 0, 0 0 4 peaks. The transition region was scanned finely on both heating and cooling. Data solely from the first counter were used for final evaluations of the short scans. Patterns for high-temperature phases were collected at 302 K over a relatively short angular range. Structural refinements were performed using the Rietveld method as implemented in the GSAS software suite [9]. Absorption corrections were based on the calculated apparent density of the powder in the capillary, and the μR values were less than 1. Linear interpolations between fixed points were used to model the background and GSAS's pseudo-Voigt function was used to fit the strongly Lorentzian peaks. All the short-scan 1 0 0, 0 1 0, 0 0 2 or 2 0 0, 0 2 0, 0 0 4 peak profiles were fitted with Lorentz function, since fit improvements when using pseudo-Voigt function occurred inconsistently.

3. Results

3.1. Transition parameters

Enthalpic DSC effects of the Verwey transition in $GdBaFe_2O_{5+\bar{w}}$ are illustrated in Fig. 1 for several levels of the oxygen nonstoichiometry $\bar{w}$. Close to the ideal composition, also the weak premonitory transition is detected. Increasing nonstoichiometry decreases transition enthalpies as well as transition temperatures. Typical of first-order phase transitions, a hysteresis is detected for the main transition, occurring within a limited temperature range where the CO and MV phases coexist. Fig. 2 illustrates that the width of the hysteresis and the temperature range of the CO/MV phase coexistence do not change in a clear manner as a function of $\bar{w}$ (see also discussion at the end of Section 3.3).

The heat-flow DSC curves have been integrated to provide both enthalpy and entropy; the latter after dividing each DSC point by its actual temperature. This treatment improves the consistency of both values with respect to the zero-line estimation, but it also means that the DSC peak is considered as being contributed from several "phases" with slightly different w, hence each having its separate transition temperature. As argued

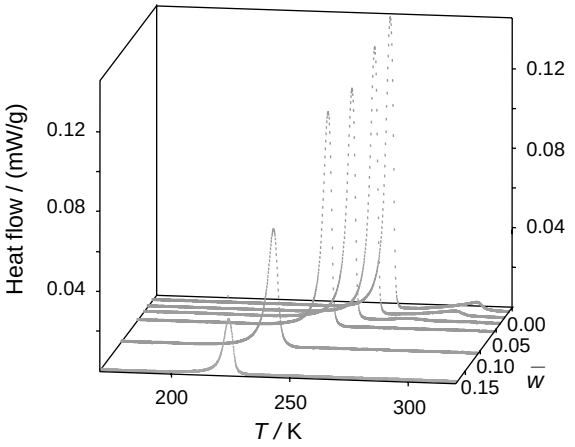

Fig. 1. Endothermic DSC peaks of the Verwey transition in $GdBaFe_2O_{5+\bar{w}}$ as observed upon warming as a function of oxygen nonstoichiometry $\bar{w} = 0.013, 0.028, 0.041, 0.061, 0.113$ and 0.181.

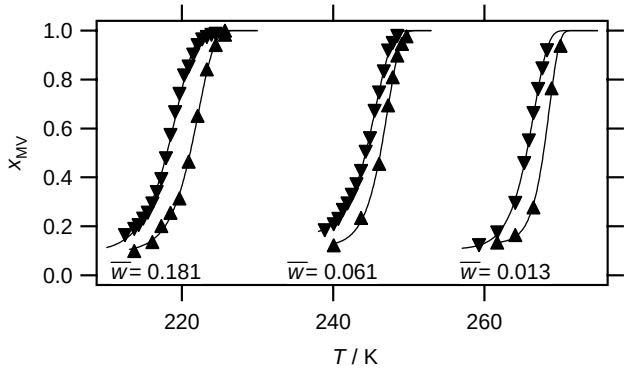

Fig. 2. Molar fraction of the MV phase and hysteresis under the Verwey-type transition in $GdBaFe_2O_{5+\bar{w}}$. Triangles indicate heating or cooling.

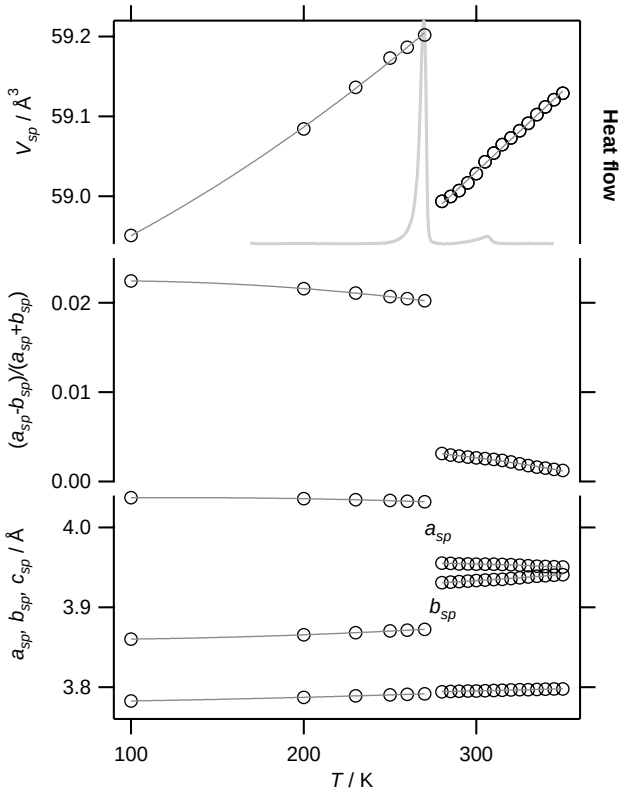

Fig. 3. $GdBaFe_2O_{4.999}$ sample; temperature dependence of the volume, orthorhombic distortion and parameters per a single-perovskite-type cell as obtained from the 2 0 0-type peak fitting.

later in Section 3.3, this is to a large extent true. In line with this approach, transition temperatures were read as peak maxima in the DSC curves (Fig. 1, as an example) and as inflection points of the SXPD-based transition sigmoidal curves (Fig. 2, as an example). SXPD was also used to follow the change in the molar volume across the transition. Fig. 3 displays cell dimensions, volume and distortion for a sample with low-oxygen nonstoichiometry. It is seen that cooling through the main transition into the CO state causes a sudden increase in volume accompanied by a profound increase in orthorhombic distortion. The discontinuity in volume at the main T_V defines the first-order character of this phase transition. Fig. 4 shows that this discontinuity persists into high levels of the oxygen nonstoichiometry, being still apparent for the sample with $\bar{w} = 0.181$. At around $\bar{w} = 0.300$ the orthorhombic distortion is still detected as increasing upon cooling, but with no discontinuity. Finally, at $\bar{w} = 0.400$ the symmetry is tetragonal throughout. The combined DSC thermal values and SXPD volume data provide thermodynamic transition parameters. These are plotted in Fig. 5 as a function of the nonstoichiometry level $\bar{w}$ and are fitted by zero-centered Lorentzians (total transition values) or Gaussians (premonitory transition values, except for the transition temperature). Although drawn as guides for eye and means to extract the values at zero nonstoichiometry, it should be noted that these curves relate to a model in Ref. [3] of probability-controlled formation of the MV $Fe^{2.5+}$ states under varied oxygen nonstoichiometry as iron pairs combined from randomly occurring divalent and trivalent ions. Both the caloric and volume changes are relatively weak, and even highly sensitive techniques such as DSC and SXPD provide data burdened with a considerable scatter. The relative uncertainty is in particular severe for the premonitory transition. No volume change exceeding standard deviations could be identified for this weak transition (Fig. 3), and it is very well possible that there is none. In addition to the mentioned limitations, there is a scatter along the composition scale owing to several factors: standard deviations of the cerimetric analyses (Table 2), inhomogeneities in the samples caused by random variations in p_{O_2} during the syntheses, and, oxidation by traces of oxygen during the storage. In this situation, reliable values are best extracted from fits to the

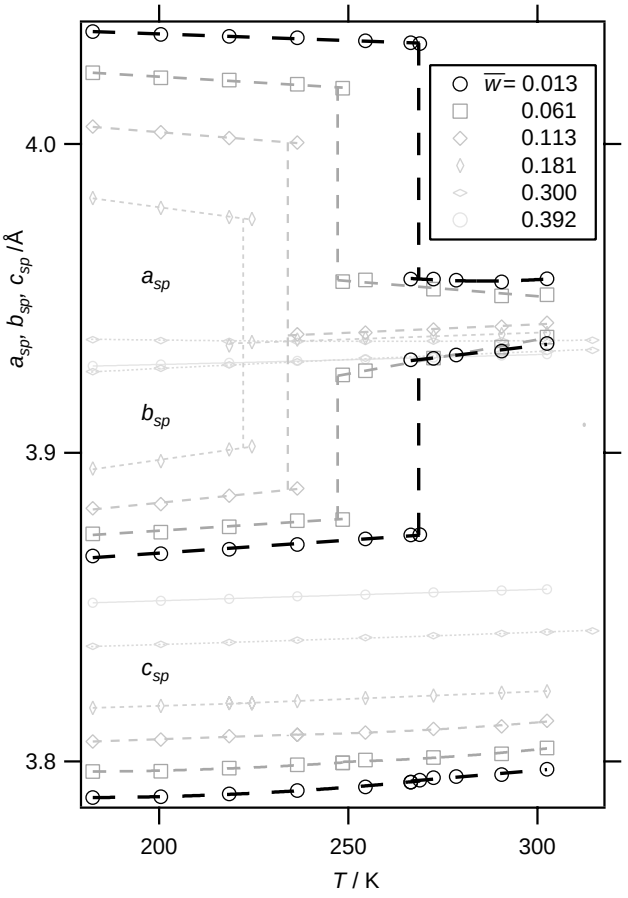

Fig. 4. $GdBaFe_2O_{5+\bar{w}}$; lattice metrics as a function of temperature T and nonstoichiometry $\bar{w}$, referring to a single-perovskite-type cell. Based on isothermal SXPD peak scans, standard deviations do not exceed the size of the symbols.

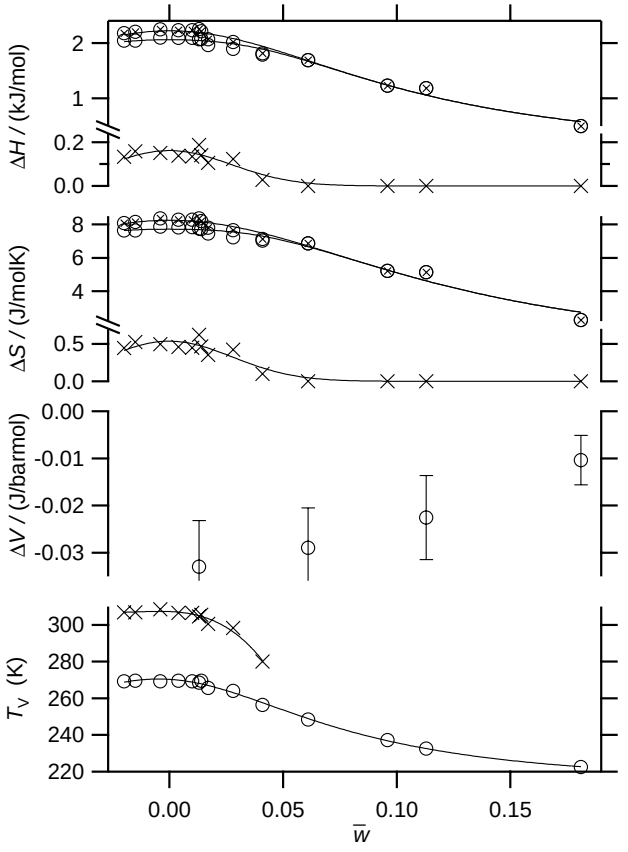

Fig. 5. Thermodynamic parameters of the premonitory (crosses) and main transition (open circles). Combined symbols refer to the total values. Unless marked otherwise, estimated standard deviations are comparable with the size of the symbols.

composition dependences. Based on such fits in Fig. 5, thermodynamic transition parameters are estimated for the ideal stoichiometry with $w = 0$ and are listed in Table 3. It is seen that the magnitudes of the transition enthalpy and entropy, as well as the transition temperatures lie between those for $R = \mathrm{Sm}$ [6] and Tb [4], in line with the same position of Gd in the lanthanoid series.

3.2. Verwey transition and the oxygen nonstoichiometry level $\bar{w}$

The mixed-valence/charge-separated cooperative system experiencing the Verwey transition is gradually being decayed by the oxygen loading $\bar{w}$. According to Mössbauer spectroscopy [3], the resulting product has normal, high-spin (HS), di- and tri-valent states of iron, which are disordered. Eventually, all iron becomes trivalent at $w = 0.500$ in an arrangement of coordination square pyramids and octahedra in equal proportion that may either be long-range ordered or disordered, depending on the temperature of the synthesis [8].

Table 3
Thermodynamics of the premonitory and main charge-ordering transition of ideal $GdBaFe_2O_{5.000}$

Transition	Premonitory	Main
T_V (K) (peak value)	307.3(10)	270.3(15)
ΔV (J bar^{-1} mol^{-1})	Practically 0	−0.034(12)
ΔH (kJ mol^{-1})	0.16(1)	2.06(1)
ΔS (J mol^{-1} K^{-1})	0.54(3)	7.72(4)
T_V (K) (peak center[a] value)	302(39)	267(3)
(dP/dT_V) (bar K^{-1})		−226(77)

[a] As given by $\Delta H/T = \Delta S$.

The first casualty of the increasing nonstoichiometry is the weak premonitory transition, which disappears via removal of the small orthorhombic deformation due to the averaging effect of the added oxygen atoms $\bar{w}$ [4,6]. It may be noted that, as a function of temperature, this minor distortion would disappear at $T_N \approx 400$ K [4]. The premonitory transition temperature and enthalpy decrease rapidly to merge with the main transition (Figs. 1

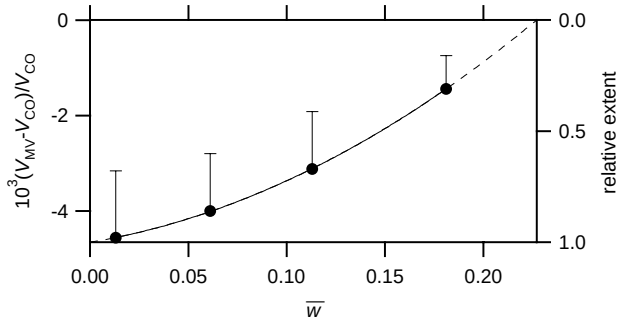

Fig. 6. Relative volume change of $GdBaFe_2O_{5+\bar{w}}$ under the main Verwey transition into the MV state. Parabolic fit as a guide for the eye.

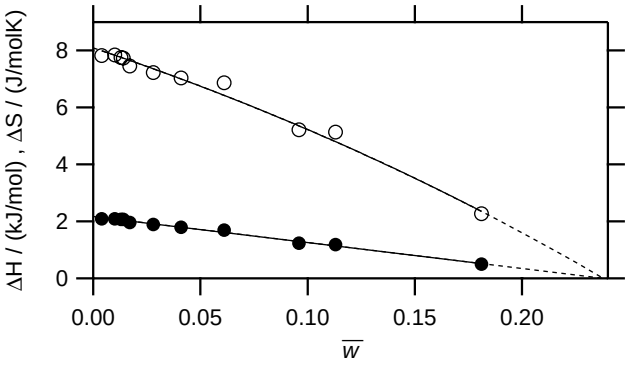

Fig. 7. The enthalpy and entropy of the main Verwey transition as a function of $\bar{w}$.

and 5) at around $\bar{w} = 0.050$. In contrast, remarkably small fractions of the MV $Fe^{2.5+}$ state are still able to drive the main transition discontinuously. In order to estimate the limit for the first-order character of the main transition, the (relative) volume change is plotted in Fig. 6 and fitted by quadratic function as a guide for the eye. Extrapolation indicates $\bar{w} \approx 0.23$ as the limit above which the transition is continuous and the content of the CO/MV states is obtainable by Mössbauer spectroscopy only [3]. The same limit is obtained for the first-order transition entropy and enthalpy: these two functions are not independent, since $\Delta H(\bar{w})/T_V(\bar{w}) = \Delta S(\bar{w})$ for every $\bar{w}$. One possibility how to introduce the composition dependence of the transition temperature, $T_V(\bar{w})$, is to consider the caloric effect being analogous to the latent heat of a freezing/thawing solution. The concave portion of the $T_V(\bar{w})$ curve (Fig. 5) is approximated in terms of depression of the freezing point of the $GdBaFe_2O_5$ solvent by the $GdBaFe_2O_6$ solute, with the transition entropy of $GdBaFe_2O_{5.000}$ (Table 3) used in the formula $T_V(\bar{w}) = T_V(0)\Delta S_{\bar{w}=0}/[\Delta S_{\bar{w}=0} - R\ln(1-\bar{w})]$. Fig. 7 shows that the $\bar{w}$ dependence of the first-order transition enthalpy for the main transition, which reflects the changing amount of the "solution" that "freezes" discontinuously, is fairly linear in the same range of $\bar{w}$, giving $\Delta H(\bar{w})/(\text{kJ mol}^{-1}) = 2.306(29) - 10.20(37)\bar{w}$. The first-order transition entropy is then $\Delta S(\bar{w}) = [\Delta H(\bar{w})/T_V(0)][1 - \ln(1-\bar{w})R/\Delta S_{\bar{w}=0}]$, which, fitted to the experimental points while having $T_V(0)$ as the only coefficient (refined to 267.9 ± 2.4 K), gives the curve in Fig. 7. Both fits are extrapolated to the level where ΔH and ΔS converge simultaneously to zero. The entropy curve can as well be approximated by a quadratic function, and this apparently also justifies the quadratic fit of the $\Delta V(\bar{w})$ function in Fig. 6.

3.3. Analysis of the nonstoichiometry distribution $X(w)$

In contrast to the sharp discontinuity of the structural transition, DSC peaks in Fig. 1 are broadened and have a distinct asymmetry. Whereas the broadening is to a large extent due to the thermal-conductivity delay of the calorimeter, the asymmetric tail directed towards low temperatures is not pertinent to this technique. Conspicuously, also the evolution of the CO/MV phases as seen by SXPD has a tail-like asymmetry, when the MV phase appears slowly and gradually upon warming. No clear dependence could be established for the width of the transition interval as a function of the oxygen content (Fig. 2), or the particle-size distribution in the sample (Fig. 8). In the following, a hypothesis is tested that such a gradual evolution appears owing to the variation of the transition temperature across the bulk of the sample caused by an asymmetric normalized distribution $X(w)$ of the local values of w in $GdBaFe_2O_{5+\bar{w}}$, where $\bar{w} = \int_{-\infty}^{+\infty} wX(w)\,dw$. Such a distribution is approximated on a stepwise function and independently evaluated from two sources originating in the SXPD data, viz., from transition curves and from Bragg-profile broadening. However, in order to do this, analyses of the instrumental and sample broadening must be performed first.

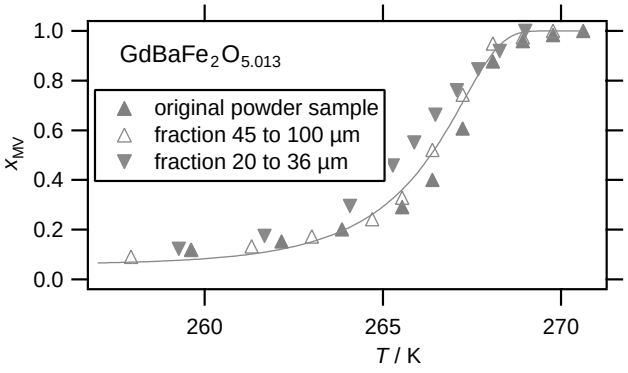

Fig. 8. Typical variations in the transition widths for $GdBaFe_2O_{5.013}$ samples with and without controlled particle size. Line is drawn as a guide for the eye, orientation of triangles designates cooling and heating.

3.3.1. Instrumental and sample broadening

Voigt decomposition according to Delhez et al. [10] of the Bragg peaks of the NIST silicon standard powder shows that the Gaussian component of the profiles is typically one-thousandth of that of the Lorentzian component. This elimination of any Gaussian "sample shadow" effect is an advantage of the single-crystal analyzer in the diffractometer setup. The instrumental broadening is therefore evaluated as Lorentzian full-width at half-maximum (FWHM) of the silicon standard peaks. Inspections of Bragg peaks of the samples reveal that in particular the $h\,0\,0$, $0\,k\,0$ and $0\,0\,\ell$ profiles area symmetric and that the direction of the asymmetry corresponds to the variations of the unit-cell parameters versus $\bar{w}$. Voigt analysis of these broadened peaks, as far as it can be done despite the asymmetry, suggests Lorentzian character with some weak Gaussian contribution for strong peaks. Lorentzian approximation is therefore adopted to determine FWHM of all "double-zero" peaks, giving the advantage of easy change to the integral breadths ($\beta = \mathrm{FWHM} \cdot \pi/2$) and direct subtractability of the instrumental breadths. Williamson–Hull plots show that the $0\,0\,\ell$ broadening consistently differs from that of the $h\,0\,0$, $0\,k\,0$ peaks for all levels of $\bar{w}$. A high intercept and (on average) zero slope for the $h\,0\,0$, $0\,k\,0$ peaks stem apparently from both the intrinsic disorder of the CO/MV states in the a,b plane and the disorder caused by the oxygen loading. In contrast, $0\,0\,\ell$ peaks have a low-lying and somewhat curved Williamson–Hull dependence with minimum around angles where the 0 0 4 Bragg peak occurs (Fig. 9). If indeed a $X(w)$ distribution across the sample causes the peak broadening, its effect should be most apparent around this minimum, and hence the 0 0 4 peak in a low-nonstoichiometry sample ($GdBaFe_2O_{5.013}$) is chosen for evaluations of the possible extent of $X(w)$.

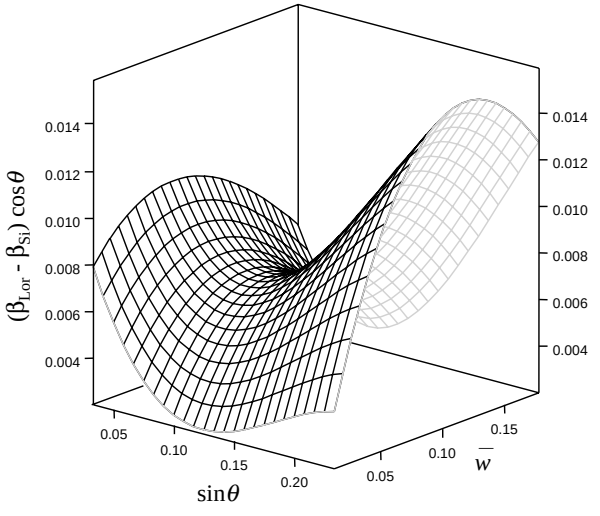

Fig. 9. Fitted surface of the Williamson–Hull plots for the $0\,0\,\ell$ Bragg reflections as a function of the oxygen content $\bar{w}$ in $GdBaFe_2O_{5+\bar{w}}$.

3.3.2. $X(w)$ from transition curves

The MV phase-content data under the transition (like those in Figs. 2 and 8) are smoothened by a cubic spline into the asymmetric sigmoid shape tailed towards lower temperatures. Twenty equally spaced temperature points are selected across the curve and assigned with w values via the dependence of T_V on $\bar{w}$ (inset in Fig. 10 bottom; here T_V refers to $x_{MV} = 0.5$ under transition). The hypothetical fractions of these 20 "phases" with somewhat differing w are obtained by differentiation at each point. Given the dependence of the unit-cell parameters a,b,c on $\bar{w}$ extracted from Fig. 4, it is possible to construct the corresponding hypothetically broadened Bragg peak of the 20-phase mixture. In Fig. 10 top, such a 0 0 4 peak is obtained by convolution of the Lorentzian instrumental-width (Fig. 10 center inset) function with the distribution of the 20 phase

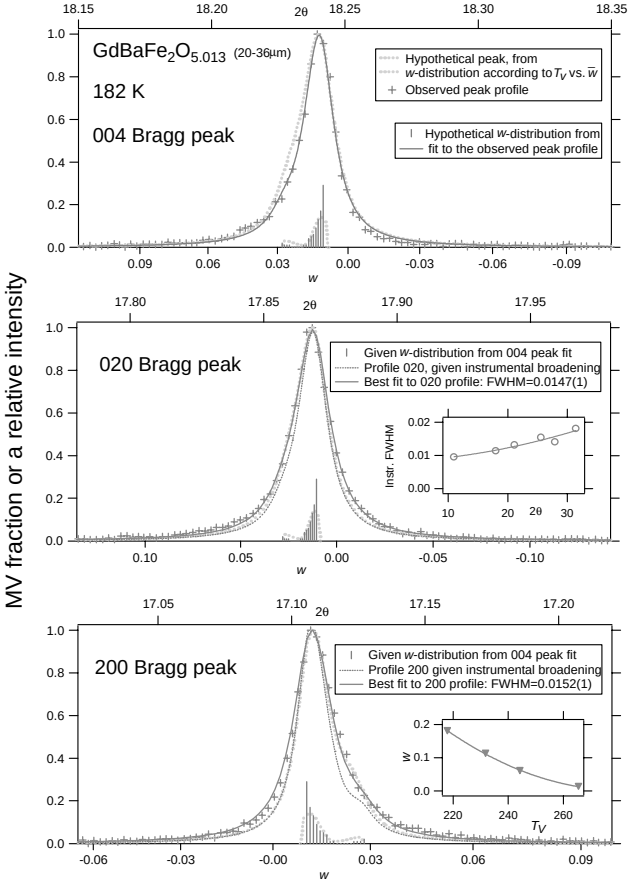

Fig. 10. Top: hypothetical 004 Bragg peak based on convolution of Lorentzian instrumental FWHM ($2\theta \approx 0.012^\circ$, middle inset) with distribution $X(w)$ obtained by assuming hat it is the sole reason behind the transition width in Fig. 8 (via $\bar{w}$ vs T_V, bottom inset). Deconvolution of the actual 0 0 4 broadening into a $X(w)$. Middle: FWHM that fits the 0 2 0 peak given the 0 0 4-based $X(w)$. Bottom: same for the 2 0 0 peak.

fractions. The actually observed profile almost exactly fills the contours of this hypothetical peak, except for a small range on the low-angle, high-w side suggesting only a small contribution of an effect other than the $X(w)$ distribution to the width of the transition curve.

3.3.3. $X(w)$ *from Bragg-profile broadening*

The oxygen content distribution is obtained by a corresponding deconvolution via fitting concentrations of the 20 phases to the observed 0 0 4 peak profile. The result covers very well the hypothetical distribution obtained from the transition curve. Being derived from the 0 0 4 peak showing least stress and strain broadening, this $X(w)$ is closest to be the true one. It is further used to model the 2 0 0 and 0 2 0 Bragg profiles (Fig. 10 center and bottom) that are somewhat broadened owing to the disorder in the a,b plane. Their FWHM values were therefore released under the fitting to see whether the 0 0 4-based w distribution is able to reconstruct the shapes of these observed peaks. This is clearly the case, hence the asymmetry of the 2 0 0, 0 2 0, 0 0 4 broadening is entirely consistent with the unit-cell parameter dependences of $\bar{w}$. Nearly identical result is obtained for the 1 0 0, 0 1 0, 0 0 2 peaks of the same pattern and for the 2 0 0, 0 2 0, 0 0 4 peak set of the same sample at 302 K. The same shape follows for samples with higher $\bar{w}$. However, the estimated FWHM of $X(w)$ increases from some 0.007 for $\bar{w}=0.013$ to about 0.015 for $\bar{w}=0.061$ and 0.030 for $\bar{w}=0.181$.

The peculiar shape of the $X(w)$ curve across the sample suggests its origin in oxidation. The main, nearly triangular part of the distribution is likely to correspond to a bulk oxygen-content inhomogeneity formed under quenching from the high-temperature equilibrium situation. This could happen both externally, from captured traces of the equilibrium atmosphere, and internally, when the cooler outer parts of the sample would oxidize at the expense of the hotter inner parts. In addition, there is an intrinsic level of the w disorder originating from point-defect equilibria that would cause a very small fraction of the O(4) oxygens (w) to be still present while oxygen vacancies were created elsewhere in the coordination polyhedron. Also related 3D-effects may be envisaged stemming from vacancy clustering and grain-surface phenomena. However, the thin tail in the $X(w)$ distribution is likely to be caused by surface oxidation during manipulation and storage. Given the extremely low equilibrium partial pressures of oxygen, which predispose the sample for oxidation, it actually is remarkable how sharp the $X(w)$ distribution is.

Analyses of the integral breadths of the Bragg peaks in patterns where the CO and MV phases occur simultaneously (Fig. 11) show a profound peak broadening at low concentrations of the MV phase, whereas the CO phase roughly maintains the peak width. Remarkably, this feature appears to be the same on both cooling and warming. Percolation effects of the newly formed MV phase are one possible cause, considering that the formation of this state is a cooperative phenomenon. Another conceivable origin of this effect would be related to the fact that T_V decreases with increasing $\bar{w}$: the most oxidized regions of the sample, where the MV phase appears first on warming and disappears last on cooling, are of smaller size than the rest of the sample. Such a picture would be consistent with effects of the surface oxidation.

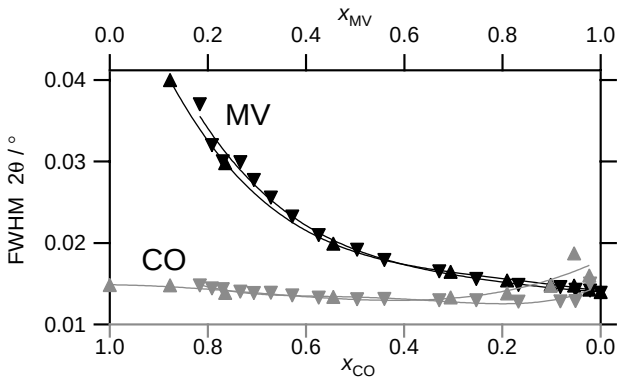

Fig. 11. FWHM values of Bragg peaks of the coexisting MV and CO phases in $GdBaFe_2O_{5.061}$ as a function of the phase content. Cooling and heating modes are distinguished by orientation of the triangles. Curves are fit as guides for the eye.

These combined results suggest that great deal, if not all, of what contributes to the coexistence of the MV and CO phases must be attributed to the variations in the oxygen content across the sample. Without this distribution in w, the transition between the CO and MV phases in the bulk of the sample would appear fairly abrupt, showing a sharp, symmetrical, practically vertical, sigmoid temperature-dependence curve. The width of this curve would be controlled only by the internally generated strain fields of the self-organizing two-phase system [11,12].

3.4. *Crystal structure of CO* $GdBaFe_2O_{4.999}$

The just described peak-profile analyses suggest that SXPD patterns of the $GdBaFe_2O_{5+\bar{w}}$ samples could be modeled by using 20 phases in appropriate concentrations. Such a multi-phase approach was indeed attempted in this special case of the CO superstructure where good resolution of weakest intensities is essential for extracting correct structure factors. For practical reasons, however, the amount of "phases" under the Rietveld refinements was reduced to nine (Table 4). Of these, only three were sufficient to model the main portion of the Bragg peak and were allowed to have unconstrained lattice parameters. The remaining six phases were assigned a common and fixed unit-cell parameter c while parameters a and b were fixed

equidistantly across the span of the orthorhombic distortion. In such a manner, the six phases were able to model the slightly enhanced background apparent in particular between the $h\,0\,0$ and $0\,k\,0$-type of Bragg peaks. The latter attribute implies two sources: a tetragonal disorder of the charge ordering and the oxidative tail of the $X(w)$ distribution. For the first three phases, highly Lorentzian parameters were obtained, and an additional improvement in the profile fit was obtained by releasing the orthorhombic microstrain anisotropy coefficients. It should be noted that the microstrain anisotropy coefficients alone, without the multi-phase model, were not able to improve the fit sufficiently. Main reasons are the asymmetric $X(w)$, counteracting dependences of unit-cell parameters, and sensitivity of the orthorhombic distortion against w. In addition, correct resolutions of some superstructure reflections depend on modeling the weak a, b disorder of the charge ordering through the phases 4–9.

Table 4
Unit-cell parameters and fractions of "phases" that model $X(w)$ and tetragonal disorder in CO $GdBaFe_2O_{4.999}$ at 100 K

"Phase"	Fraction	a (Å)	b (Å)	c (Å)
1	0.530(18)	8.07606(3)	3.86005(2)	7.56511(3)
2	0.350(17)	8.07331(18)	3.86129(8)	7.56757(15)
3	0.100(5)	8.05266(87)	3.86573(58)	7.57546(58)
4	0.0050(4)	8.00	3.90	7.57
5	0.0025(4)	7.98	3.91	7.57
6	0.0036(4)	7.96	3.92	7.57
7	0.0034(4)	7.94	3.93	7.57
8	0.0039(4)	7.92	3.94	7.57
9	0.0017(3)	7.90	3.95	7.57

The comparison of the observed and fitted SXPD pattern is shown in Fig. 12. A number of superstructure Bragg reflections rises above the background in this high-flux, high-resolution pattern. Altogether 21 CO superstructure peaks are visually discerned in the angular range 8–29° 2θ. All correspond to reflection conditions of the $TbBaFe_2O_5$-type [4] of the charge ordering. A section of the pattern with 100× magnified intensity in the inset of Fig. 12 illustrates resolution of several such superstructure peaks. Since the unit-cell parameters of the first two phases refined to rather close values whereas the third phase drifted somewhat away, only phases 1 and 2 were considered to be fully CO in the refinements. This means that the full 3D charge ordering was assumed to concern 88% of the sample. Atomic coordinates of phases 1 ad 2 were constrained to be the same and are listed in Table 5 together with the figures of merit of the refinement. Atomic coordinates of phase 3 were released in such a manner that allows to model the average structure with no 3D charge ordering (but still having a high degree of charge separation): The z coordinate of O(1) was fixed to zero, the z coordinates of O(2) and O(3) were constrained to be equal and subsequently refined to 0.3175(29), the x coordinate of O(1) was fixed to zero, and one common z coordinate of Fe was adopted and subsequently refined to 0.2747(14). For phases 4–9, all atoms were fixed in positions corresponding to those refined for the $GdBaFe_2O_{5.113}$ sample at 182 K, vide infra.

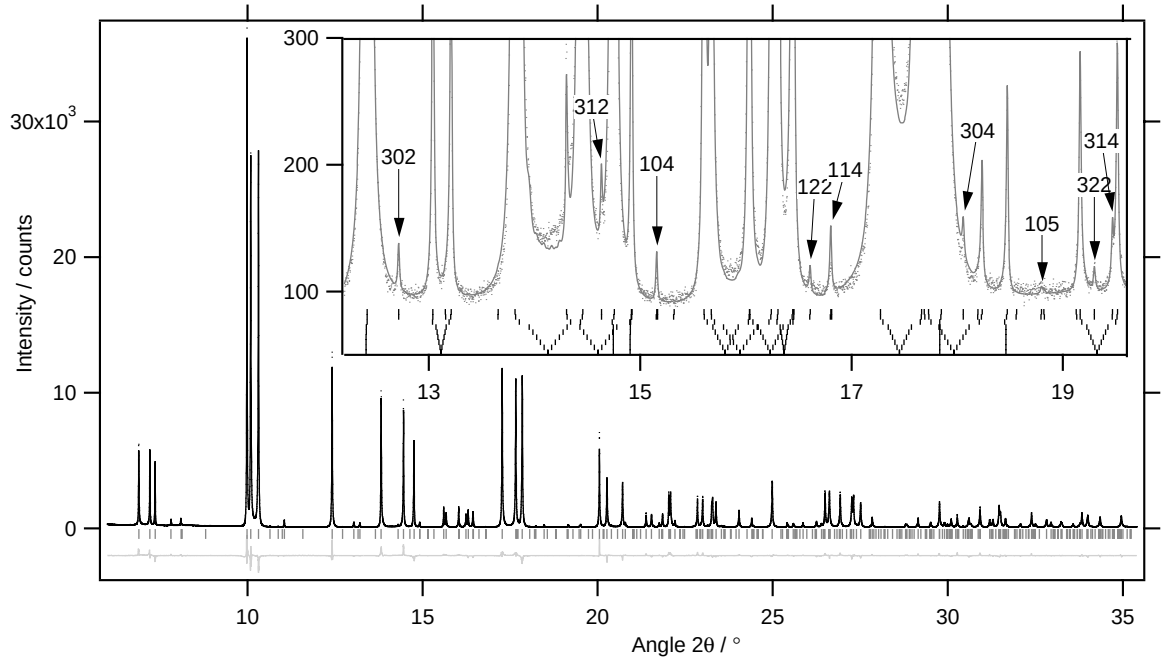

Fig. 12. Rietveld-refinement profile of SXPD data for $GdBaFe_2O_{4.999}$ at 100 K. Positions of the Bragg reflections of the CO phases 1 and 2 (Table 4) are marked in the set of vertical bars. An example of the superstructure reflections is in the inset.

The unit cell of the refined CO structure is shown in Fig. 13. The refined coordinates, listed in Table 5, are in reasonable agreement with those of the Tb version obtained from powder neutron diffraction. The same principal mechanism of charge ordering is implied. Within the symmetry constraints of the space group *Pmma*, both O(1) and O(3) are allowed to approach one of two iron atoms in an ordered manner, and that atom becomes trivalent. The calculated bond distances and bond valences are given in Table 6. Comparison with powder neutron diffraction data for $TbBaFe_2O_5$ in Table 7 indicates the same high degree of charge ordering in terms of bond valences of the iron atoms. Furthermore, for both Gd and Tb versions the same structural compromises discussed in Ref. [6] are adopted, viz., underbonding of the rare-earth atom and overbonding of O(1). The SXPD refinement data, however, seem to suggest a lesser degree of charge separation for the Fe–O(3)–Fe joints along the expanded *a*-axis and a higher one for the Fe–O(1)–Fe apices. While the significance of the neutron- and synchrotron-based distances must be weighted by the scattering factors of oxygen for neutrons and X rays, it may be noted that the shorter apex bond distance of 1.82 Å is not impossible as it would still carry only 0.85(3) valence units. The charge separation in Tables 6 and 7 appears inclined towards trivalence, but this is largely due to the fact that bond-valence coefficients referring to room temperature are used for the low-temperature contracted structure. The separation by 0.75 valence units of iron is hence quite symmetrical. According to Mössbauer spectroscopy, practically only two iron valence states are present at low-temperatures in CO $TbBaFe_2O_5$ [4]. The less than unity charge separation cannot therefore be attributed to a presence of residual disordered MV or any other valence and spin state of iron. Either this is a bond-valence artifact imposed for example by a structural compromise involving the other atoms in the structure (and the actual valence separation of iron is practically 1.00), or the charge separation is indeed less than complete in terms of charges of the two iron states. The transition entropy (Table 3) being 0.72 of the theoretical [5] value of $2R\ln 2$ may speak in favor of the latter explanation. Also for magnetite, the reported low transition entropies may correlate with the bond-valence charge separation of only 0.4 reported for the recently determined crystal structure of its CO state [13]. More systematic data are presently being collected to reveal how the charge

Table 5
Refinement results for CO $GdBaFe_2O_{4.999}$ at 100 K

Unit-cell data			Statistics	
Space group	*Pmma*		R_{wp}	0.067
Phase 1	Table 4		R_p	0.053
Phase 2	Table 4		N_{vars}	41
Atom	Site	*x*	*y*	*z*
Gd	2*c*	0	0	0.5
Ba	2*a*	0	0	0
Fe(1)	2*f*	1/4	1/2	0.2491(3)
Fe(2)	2*f*	3/4	1/2	0.2701(3)
O(1)	2*f*	1/4	1/2	0.0086(15)
O(2a)	2*e*	3/4	0	0.3102(16)
O(2b)	2*e*	1/4	0	0.3125(17)
O(3)	4*j*	0.0072(13)	1/2	0.3053(4)

Note. Atomic coordinates constrained equal for phases 1 and 2. Displacement parameters constrained all equal for phases 1–3 and refined to $U_{iso} = 0.00022(5)$ Å^2.

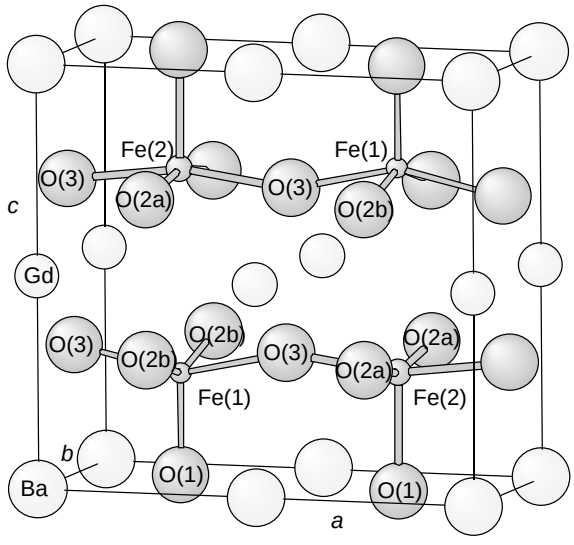

Fig. 13. The unit cell of CO $GdBaFe_2O_5$.

Table 6
Bond distances (in Å) and bond valences for CO $GdBaFe_2O_{4.999}$ at 100 K

Atom	Gd	Ba	Fe(1)	Fe(2)	Oxygen BV
O(1)		$4 \times 2.7939(2)$	$1 \times 1.820(13)$	$1 \times 2.108(13)$	2.22(4)
O(2a)	$2 \times 2.478(7)$	$2 \times 3.096(9)$		$2 \times 1.954(2)$	1.98(3)
O(2b)	$2 \times 2.468(7)$	$2 \times 3.109(9)$	$2 \times 1.989(4)$		1.96(3)
O(3)	$4 \times 2.429(2)$	$4 \times 3.010(2)$	$2 \times 2.007(9)$	$2 \times 2.1094(11)$	1.92(3)
Metal BV	2.83(3)	2.01(2)	2.95(7)	2.22(4)	

Table 7
Bond distances (Å) and bond valences for CO $TbBaFe_2O_{5.012}$ at 70 K

Atom	Tb	Ba	Fe(1)	Fe(2)	Oxygen BV
O(1)		$4 \times 2.7864(1)$	$1 \times 1.895(9)$	$1 \times 2.046(9)$	2.15(3)
O(2a)	$2 \times 2.434(2)$	$2 \times 3.140(3)$		$2 \times 1.962(1)$	1.98(1)
O(2b)	$2 \times 2.469(3)$	$2 \times 3.094(3)$	$2 \times 1.975(1)$		1.98(1)
O(3)	$4 \times 2.404(1)$	$4 \times 3.031(1)$	$2 \times 1.965(3)$	$2 \times 2.134(4)$	1.94(1)
Metal BV	2.88(1)	1.99(1)	2.95(3)	2.19(2)	

Note. Calculated from powder-neutron diffraction data in Ref. [4]. The O(4) oxygens ($\bar{w} = 0.012$) are neglected.

separation, as well as the valence and spin-state contents, vary across the $R\mathrm{BaFe_2O_5}$ series.

3.5. Crystal structure as a function of oxygen nonstoichiometry $\bar{w}$

The low-temperature 3D order is a superstructure to the double-cell perovskite-type superstructure. Its extremely weak Bragg reflections disappear rapidly under increasing oxygen nonstoichiometry, leaving only the orthorhombic distortion to witness about the continued separation of charges in one dimension along the *a*-axis.

Already a minor oxygen nonstoichiometry of $\bar{w} = 0.013$ suppresses the CO superstructure SXPD intensities to about a half of those expected for a full charge order. Such data are no longer refinable in the CO model, and the structure refinement of this low-temperature phase is therefore based on the same average double-volume perovskite cell used for the other oxygen-loaded samples. Such a cell is shown in Fig. 14. It illustrates the refinement model designed to take care of the disorder due to the nonzero occupancy of the O(4) site. Since no evidence has been obtained for any Ba/Gd site mixing [8], the O(4) atom in the Gd layer would appear in a too close contact to the two iron neighbors and the oxygens O(2) and O(3). The real structure must locally adopt more appropriate bond distances, and this is modeled in the Rietveld refinements by introducing a split-site for the iron atom (whereas not for the weakly scattering oxygens) where the normal Fe site $\frac{11}{22}z$ had occupancy $1 - w$ and the Fe′ site $\frac{11}{22}0.25$ had occupancy $\bar{w}$. As noted in Section 3.3, the oxygen loading $\bar{w}$ leads to increased Bragg peak broadening. This to a large extent overshadows the effects of the oxygen-content distribution across the sample under Rietveld refinements, and the data offer less support for the multi-phase model that was so successful for extracting intensities of the CO superstructure. The distribution of the unit-cell parameters across the sample is to a some degree taken care of by releasing the S_{HKL} anisotropy coefficients of Stephens [14], as adopted in the profile function CW4 in Ref. [9].

The refined structure data for nonstoichiometric $\mathrm{GdBaFe_2O_{5+\bar{w}}}$, at temperatures corresponding to

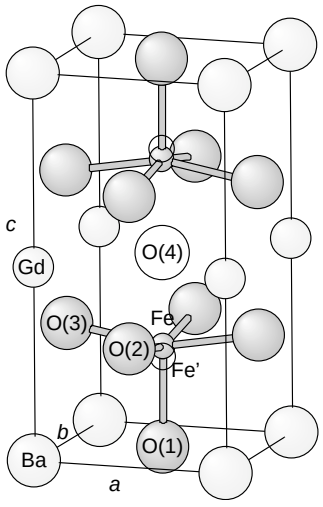

Fig. 14. Model of the oxygen nonstoichiometry in the unit cell of the average structure of $\mathrm{GdBaFe_2O_{5+\bar{w}}}$.

occurrences of CO and MV phases in low-$\bar{w}$ samples, are listed in Tables 8 and 9, respectively. Examples of the calculated and refined patterns for both temperatures are shown in Fig. 15. A general feature not affected by the temperature is seen in a marked increase of atomic displacement factors as a function of increasing $\bar{w}$. Oxygens are prone in particular, and this suggests contribution from the local disorder introduced by the partial filling of the O(4) site. The same trend is observed for the figures of merit of the refinements.

It is intuitive that the nonstoichiometry-induced disorder has a maximum at $\bar{w} = 0.500$, which corresponds to a random mixture of equal amounts of coordination square pyramids and octahedra, both hosting trivalent iron. In contrast, the $\bar{w} = 0.000$ composition refers to the square-pyramidal coordination hosting equal amounts of formally di- and trivalent iron, either in the CO or the MV state. Mössbauer spectroscopy [3] shows that the MV ion $Fe^{2.5+}$ is progressively decayed by the increasing oxygen nonstoichiometry ($\bar{w}$), in tact with decreasing availability of the minority Fe^{2+} ions capable of mixing 1:1 with a neighboring Fe^{3+} ion. A parallel and identical decrease

Table 8
Structure refinement parameters for $GdBaFe_2O_{5+\bar{w}}$ at 182 K

	$\bar{w}$					
	0.013	0.061	0.113	0.181	0.300	0.392
R_{F^2}	0.038	0.034	0.043	0.030	0.042	0.048
N_{obs}	78	103	96	96	171	98
λ (Å)	0.60044	0.60044	0.60044	0.50019	0.50086	0.50086
Unit-cell parameters						
a (Å)	4.03480(1)	4.02136(1)	4.00420(1)	3.98360(1)	3.93602(1)	3.92791(1)
b (Å)	3.86515(1)	3.87217(1)	3.88098(1)	3.89546(1)	3.92546(1)	
c (Å)	7.57386(2)	7.59056(2)	7.61115(2)	7.63557(2)	7.67318(1)	7.70239(2)
Volume (Å^3)	118.115(1)	118.195(1)	118.279(1)	118.488(1)	118.556(1)	118.836(1)
Atom positions	*Pmmm*	*Pmmm*	*Pmmm*	*Pmmm*	*Pmmm*	*P4/mmm*
z(Fe)	0.2600(2)	0.2603(2)	0.2596(2)	0.2599(3)	0.2594(2)	0.2584(3)
z[O(2)]	0.3114(4)	0.3101(5)	0.3071(4)[a]	0.3062(4)[a]	0.3014(2)[a]	0.2993(4)
z[O(3)]	0.3088(4)	0.3085(5)	0.3071(4)[a]	0.3062(4)[a]	0.3014(2)[a]	
Displacement parameters $100 \times U_{iso}$ (Å^2)						
Gd,Ba	0.03(1)	0.19(1)	0.30(2)	0.74(1)	0.51(1)	0.99(1)
Fe	0.28(3)	0.15(2)	0.16(3)	0.64(3)	0.03(1)	0.39(2)
Oxygens	0[b]	0.18(9)	0.42(9)	0.71(9)	0.88(4)	1.82(7)

Pmmm. Gd $00\frac{1}{2}$, Ba 000, Fe $\frac{11}{22}z$ with fraction $1-\bar{w}$, Fe′$\frac{11}{22}0.25$ with fraction $\bar{w}$. O(1) $\frac{11}{22}0$, O(2) $\frac{1}{2}0z$, O(3) $0\frac{1}{2}z$, O(4) $\frac{111}{222}$ with fraction $\bar{w}$. *P4/mmm*: Same atom positions as above, except that O(2) ≡ O(3).

[a] Refined to nearly equal values and was hence constrained: z[O(2)] = z[O(3)].

[b] Fixed to a value from the trend according to $\bar{w}$.

Table 9
Structure refinement parameters for $GdBaFe_2O_{5+\bar{w}}$ at 302 K

	$\bar{w}$					
	0.013	0.061	0.113	0.181	0.300	0.392
R_{F^2}	0.039	0.048	0.036	0.042	0.050	0.054
N_{obs}	41	43	26	44	111	41
λ (Å)	0.60044	0.60044	0.60044	0.50086	0.50086	0.50086
Unit-cell parameters						
a (Å)	3.95456(1)	3.94878(1)	3.94035(1)	3.93745(1)	3.93568(2)	3.93089(1)
b (Å)	3.93381(1)	3.93575(1)			3.93196(2)	
c (Å)	7.59170(2)	7.60477(2)	7.62326(2)	7.64293(1)	7.68212(3)	7.70955(2)
Volume (Å^3)	118.100(1)	118.189(1)	118.361(1)	118.492(1)	118.880(1)	119.127(1)
Atom positions	*Pmmm*	*Pmmm*	*P4/mmm*	*P4/mmm*	*Pmmm*	*P4/mmm*
z(Fe)	0.2642(2)	0.2638(3)	0.2632(3)	0.2617(2)	0.2572(3)	0.2570(4)
z[O(2)/O(3)]	0.3053(5)	0.3072(5)	0.3054(5)	0.3057(3)	0.3019(3)	0.3018(4)
Displacement parameters $100 \times U_{iso}$ (Å^2)						
All atoms	0.20(3)	0.04(3)	0.20(3)	0.71(2)	0.60(1)	0.77(2)

Pmmm. Gd $00\frac{1}{2}$, Ba 000, Fe $\frac{11}{22}z$ with fraction $1-\bar{w}$, Fe′$\frac{11}{22}0.25$ with fraction $\bar{w}$. O(1) $\frac{11}{22}0$, [O(2) $\frac{1}{2}0z$, O(3) $0\frac{1}{2}z$] z constrained equal, O(4) $\frac{111}{222}$ with fraction $\bar{w}$. *P4/mmm*. Same atom positions as above, except that O(2) ≡ O(3).

occurs for concentrations of the valence- and spin-states that constitute the CO arrangement [3]. The oxygen nonstoichiometry disrupts the CO/MV system as a whole, in favor of an arrangement where di- and trivalent iron HS states are disordered. These states are generally not identical with those that constitute the CO arrangement under charge trapping at low temperatures [3].

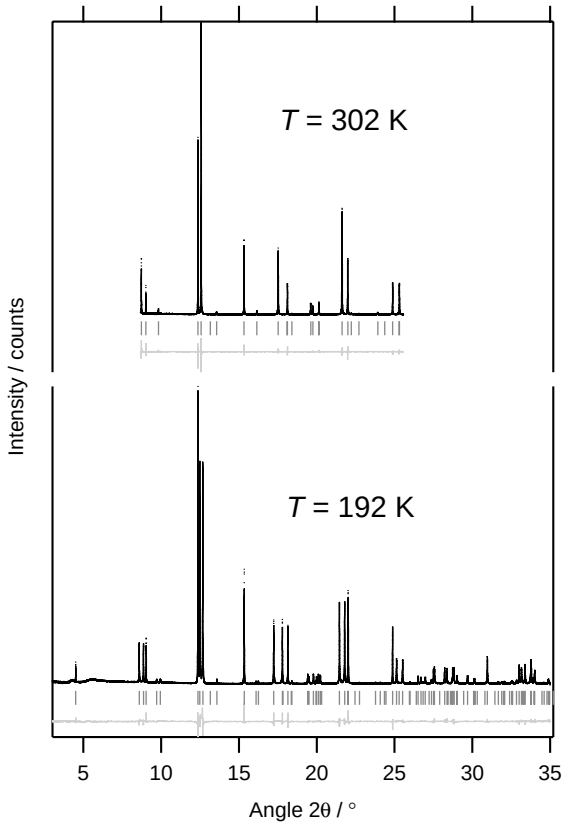

Fig. 15. Observed, refined and difference data for Rietveld refinements of $GdBaFe_2O_{5.113}$ at 182 K (charge separated; bottom) and 302 K (mixed valence; top).

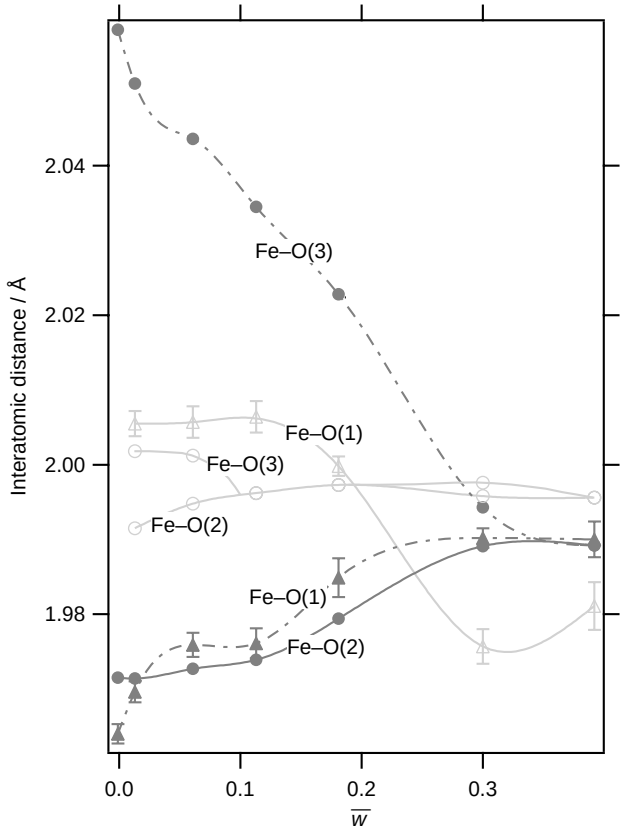

Fig. 16. Iron–oxygen distances in square pyramidal coordinations of $GdBaFe_2O_{5+\bar{w}}$. Curves as guides for the eye are in black for 182 K and gray for 302 K. Standard deviations correspond to the size of the symbols unless marked otherwise.

From the refined unit-cell parameters in Tables 8 and 9 it can be extracted that the increased O(4) occupancy $\bar{w}$ causes a contraction in the a, b area and an expansion along c. The latter occurs due to the size difference of Ba and Gd as the iron atom tends to equalize the bond length towards O(4) in the Gd layer with the bond length towards O(1) in the Ba layer (Fig. 14). The a, b contraction can simply be attributed to the oxidation of the larger Fe^{2+} ion into the smaller Fe^{3+}.

Given that octahedral coordinations of iron are fixed in the applied refinement model, variations in the refined atomic parameters reflect largely the changes within the coordination square pyramids. Evolution of such iron–oxygen bond distances as a function of $\bar{w}$ is illustrated in Fig. 16 for both the low-temperature and high-temperature phase. The common feature is their eventual equalizing as concentration of Fe^{3+} increases. In the low-temperature phase, the iron-oxygen distances become practically equal above $\bar{w} \approx 0.35$. This is also the level where Mössbauer spectroscopy [3] ceases to see any traces of the CO/MV states and where the phase contains only the disordered HS integer valence states Fe^{3+} and Fe^{2+}. The gradual charge separation below this level of oxygen nonstoichiometry is associated with an elongation of Fe–O(3) and a contraction of Fe–O(1). The Fe–O(3) bond expands in parallel with the increasing orthorhombic distortion, the Fe–O(1) bond contracts in parallel with the decreasing occupancy of the O(4) site by the large oxygen ion. Both distances are actually averages of two locally differing bond lengths of the charge-separated couple: a long one to Fe^{2+} and a short one to Fe^{3+}, as judged from distances of O(1) and O(3) from Fe(1) and Fe(2) in the 3D CO structure in Table 6. The randomly occurring added oxygens would decrease the average differences of these two pairs of unequal bonds and average them further to the refined middle lengths Fe–O(1) and Fe–O(3) within the double-volume cell, by removing the glide plane of the quadruple-volume CO cell. Because of this double averaging, it is not possible to extract the individual bond lengths referring to the local charge ordering (as in Fig. 13) as a function of oxygen nonstoichiometry. This also prevents a meaningful bond-valence analysis of the low-temperature phases.

Bond valences are better defined within the model of the high-temperature nonstoichiometric structure in Fig. 14. The evolution of the bond valences, calculated from data in Table 9, is shown in Fig. 17. It is seen that

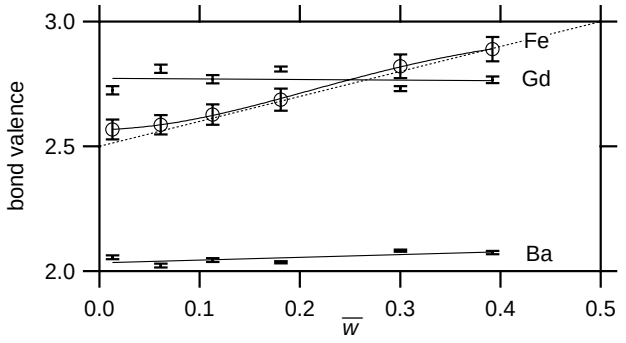

Fig. 17. Bond valences at 302 K calculated from refined data in Table 9. Dotted line represents the formal iron valence dictated by $\bar{w}$.

Ba is overbonded and Gd underbonded, as expected when these two differently sized atoms are located at positions that would be equivalent in the primitive lattice of single-perovskite. The average bond valence of iron follows roughly the linear trend of the formal valence dictated by composition, but a deviation towards higher values is seen when $\bar{w}$ approaches zero. This should be attributed to the increasing content of the MV state: according to the Virial theorem [15], $Fe^{2.5+}$ has smaller volume than the corresponding average of the HS di- and trivalent ions, and it gives therefore a falsely high bond valence when a composition-weighted average of the Fe^{2+} and Fe^{3+} bond-valence coefficients is used. A similar although statistically not significant deviation occurring around $\bar{w} = 0.30$ could possibly, together with thereby occurring orthorhombic distortion, be indicative of another valence mixing. Overall, the very well matched average iron valence confirms the validity of the refinement model composed of the contributions from the Fe′ site centering the octahedra and the Fe site in the square pyramids. It is mainly the proportion of these two sites that makes for the change in the average iron valence in Fig. 17; the individual valences vary less as a function of $\bar{w}$. As follows from Fig. 16, the average bond distance in the square pyramids even slightly increases with the initial oxygen loading, instead of decreasing that would be required by the gradual introduction of the smaller Fe^{3+} ion. However, this is only the inverse of the MV size effect mentioned above, when the $Fe^{2.5+}$ ion is being replaced by the, on average, larger integer-valence ions. First when most of the MV state is converted to the HS integer states, viz., around the level of $\bar{w} = 0.20$, a contraction of Fe–O(1) sets in (Fig. 16). Finally, it may look surprising that the inserted oxygen O(4) does not increase the bond valence of Gd. This is because the bulky oxygen atom separates Gd farther away from its eight oxygen contacts, while contributing little to the Gd bond valence owing to the large distance in the a, b plane, which is dictated by the size of the Ba atom.

4. Discussion

A number of compounds exist of the Robin and Day [16] class I of mixed valence, in which different integer valence states of same element occur in different structural environments, having different electronic energy levels. Well-known $AgAgO_2$ and Pb_2PbO_4 are typical examples of such very distinctly CO arrangements. In contrast to these classically integer valences, mixed valence of class III implies two or more atoms sharing an electron. In particular, semi-integer valence states are very common and occur in both crystalline and amorphous solids, both in molecules and infinite bond networks. Reported failures to discern the participating integer valences by registering the electron at one of the two atoms on the time-scale as short as a femtosecond suggest that this is a phenomenon of chemical bond rather than electron hopping, oscillation or fluctuation. In line with this view, bond distances on average shorten upon entering into the MV state, as manifested in the volume decrease. The implied 1/4 filling of a molecular orbital makes the "conjugation" effect of semi-integer valences much weaker than the 1/2 filling in, say, benzene. The formation of the MV states in the $Fe_2^{2.5+}O_5\}^{5-}$ network is entropy driven and scales with thermal energy (Table 3). Term vibronic coupling is accordingly preferred for description of interactions leading to the MV states when molecules are concerned. As noted by Mott [17], it is rare that these two extreme cases, CO and MV, are able to convert to each other as a function of temperature. The double-cell perovskites, exemplified here by $GdBaFe_2O_5$, are remarkable not only by exhibiting this property, but also by the extraordinarily high extent of the resulting charge separation and ordering. Comparisons with data on magnetite [13,18] suggest that the high degree of charge separation is what correlates with the ability to withstand the high levels of nonstoichiometry perturbations. Since the nonstoichiometry and hence the different iron states are distributed randomly, at least for the most part of the homogeneity range, methods of local focus, such as Mössbauer spectroscopy, rather than those of long-range order, will be essential to account for the valence and spin states that would enter any statistical thermodynamic description of the CO/MV phases and their mutual conversion.

Given the energy scale, the negative volume change and the endothermic thermal effect under the transition into the MV state, melting of ice is perhaps a good analogy. In the title compound, an ice of charges Fe^{2+} and Fe^{3+} melts into an organized liquid with charges $Fe^{2.5+}$. The charge ice maintains the large volume due to the Coulombic repulsion (or due to the asymmetry of the bond potential), the water ice due to fully oriented hydrogen bonds. The charge liquid has aligned $Fe^{2.5+}$ couples, the water liquid has two-coordinated ring

clusters with proton ordering in one direction around the ring [19]. In both liquids, this permits strong electronic delocalizations, on the Mössbauer scale (the charge liquid) [3] or on the NMR scale (the water liquid) [19]. Nonstoichiometry decreases the freezing point T_V of the charge liquid, a solute decreases the freezing point of the water liquid.

Acknowledgments

Experimental assistance from the staff of the Swiss-Norwegian Beam Lines at ESRF is gratefully acknowledged.

References

[1] J. Lindén, A. Kjekshus, P. Karen, J. Miettinen, M. Karppinen, J. Solid State Chem. 139 (1998) 168.
[2] P.M. Woodward, P. Karen, Inorg. Chem., submitted.
[3] J. Lindén, P. Karen, A. Kjekshus, J. Miettinen, T. Pietari, M. Karppinen, Phys. Rev. B 60 (1999) 15251.
[4] P. Karen, P.M. Woodward, J. Lindén, T. Vogt, A. Studer, P. Fisher, Phys. Rev. B 64 (2001) 214405.
[5] E.J. Verwey, P.W. Haayman, F.C. Romeijn, J. Chem. Phys. 15 (1947) 181.
[6] P. Karen, P.M. Woodward, P.N. Santhosh, T. Vogt, P.W. Stephens, S. Pagola, J. Solid State Chem. 168 (2002) 11.
[7] J.P. Shepherd, R. Aragón, J.W. Koenitzer, J.M. Honig, Phys. Rev. B: Condens. Matter 32 (1985) 1818.
[8] P. Karen, P.M. Woodward, J. Mater. Chem. 9 (1999) 789.
[9] A.C. Larson, R.B. Von Dreele, General Structure Analysis System (GSAS), Los Alamos National Laboratory Report LAUR 2000, pp. 86–748.
[10] R. Delhez, T.H. de Keijser, J.I. Langford, D. Louër, E.J. Mittemeijer, E.J. Sonneveld, in: R.A. Young (Ed.), The Rietveld Method, IUCr, Oxford University Press, Oxford, 1993, pp. 132–166.
[11] E.B. Smith, Phys. Chem. Solids 9 (1959) 182.
[12] N.D. Mathur, P.B. Littlewood, Solid State Commun. 119 (2001) 271.
[13] J.P. Wright, J.P. Attfield, P.J. Radaelli, Phys. Rev. Lett. 87 (2001) 266401.
[14] P.W. Stephens, J. Appl. Crystallogr. 32 (1999) 281.
[15] J.B. Goodenough, J. Alloys Compd. 262–263 (1997) 1.
[16] M.B. Robin, P. Day, Adv. Inorg. Chem. Radiochem. 10 (1967) 247.
[17] N.F. Mott, Philos. Mag. B 42 (1980) 327.
[18] J.P. Shepherd, J.W. Koenitzer, R. Aragón, J. Spałek, J.M. Honig, Phys. Rev. B 43 (1991) 8461.
[19] R. Ludwig, F. Weinhold, J. Chem. Phys. 110 (1999) 508.